

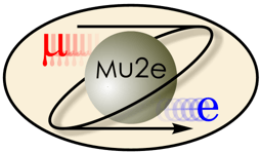

Support systems of Mu2e DS Tracker

Batavia, September 23, 2016

Student:
Gabriele Taddei

Supervisor:
Giuseppe Gallo

Fermilab Summer Intern 2016

Abstract

This report describes the activities carried out at Fermilab related to the ongoing Mu2e experiment. I was involved, in particular, in the development of preliminary designs of one of the main particles detector.

During the initial phase, I focused on understanding the existing models along with the interfaces, the requirements and the specifications. Afterwards, I was assigned the following tasks:

1. Development of electrical and gas systems conceptual designs;
2. Analytical evaluation of mounting planes uncertainty;
3. Check of contact pressure studies.

To accomplish the first task, I had to work directly with the electrical experts, going back and forth multiple times through individual and weekly group meetings. Most of the conceptual design was accomplished while only residual issues are still work in progress. Regarding the second task, I evaluated the analytical uncertainties related to mounting planes, implementing existing concepts used for a different application. The target of the third task was to verify contact pressure studies using established analytical models.

I would like to thank many people: at first, Giuseppe Gallo, my supervisor, for his availability, his patience and the opportunity to be involved and integrated into the work team, dealing directly with physicists, engineers and external collaborators. It was an irreplaceable opportunity to build up work experience, open my mind and sharpen my language skills.

Then, I'd like to thank Aseet Mukherjee, Vadim Rusu and George Ginther, whose collaboration was so precious to collect information about support systems and interface devices; Luke Martin, John Rauch, Russell Rucinski and Barbara Kristen, for their support, especially during the very first days.

I express deep gratitude towards Giorgio Bellettini, Emanuela Barzi and Simone Donati, for the organization of a unique and lifelong experience.

And thanks to my family, without which none of this would have been possible.

Contents

Chapter 1

Introduction

Before describing the tracker design, an introduction to Mu2e experiment is necessary.

1.1 Mu2e goal

The aim of Mu2e experiment is the observation of a muon which, interacting with a nucleus, changes only into an electron, phenomenon known as Charged Lepton Flavor Violation[1] (CLFV). The outcome of the experiment will help physicists in any case: if the change is obtained, some plausible theories about sub-particle physics will be denied; if it doesn't happen, many existing models have to be radically rethought.

1.2 Mu2e apparatus

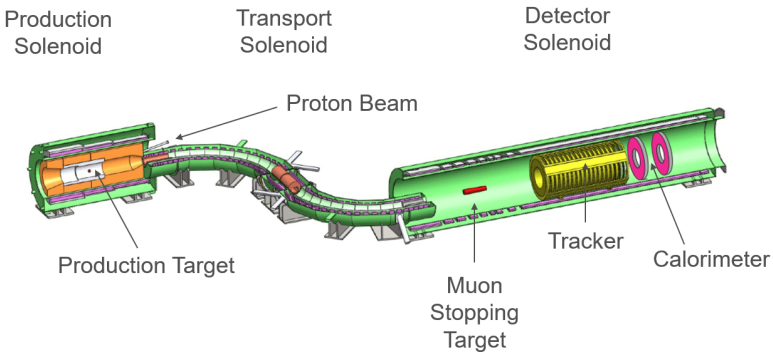

Figure 1.1: Mu2e machinery layout.

[1]The process according to which a particle changes into a different one is called Flavor Violation. Given that muons and electrons are both leptons with electrical charge, we speak about Charged Lepton Flavor Violation.

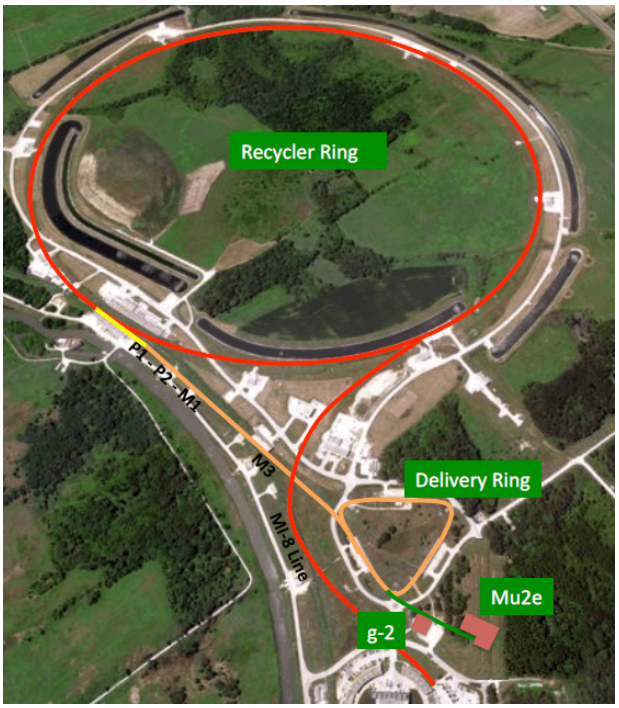

Figure 1.2: Accelerator complex, which supplies proton beam to Mu2e apparatus.

In fig.1.1 main components of Mu2e apparatus are reported [1]. A proton bunch, taken out from Recycler Ring (fig.1.2), is transported to Delivery Ring (once named *Fermilab Debuncher*). Here, a 8 GeV proton beam is extracted in pulses[2] of $\approx 3 \times 10^7$ protons every 1.7 µs and deliverd to Production Solenoid (PS), hitting the Production Target (PT): the process generates pions which decay into muons[3].

Transport Solenoid (TS) collects and transfers muons to Detector Solenoid (DS), where they hit the aluminum Muon Stopping Target (MST) and change into electrons, whose momentum is $\approx 105\,\mathrm{MeV/c}$. The DS contains a calorimeter, that evaluates electrons energy, position and arrival time, and a tracker, which measures their trajectory and momentum. The presence of the tracker is fundamental, since the calorimeter doesn't distinguish, with tolerable reliability, conversion electrons from neutrons, photons or other potential sources. After all, tracker resolution has to be sufficient in order to separate signal electrons from DIO[4] electrons.

Inside DS, uniform 1 T magnetic field and 10^{-4} Torr pressure are required.

[2]Employing a delayed live window, the pulse beam allows for the elimination of prompt background.

[3]As single event sensitivity of Mu2e experiment is 2.4×10^{-17}, about 10^{20} protons on target are necessary.

[4]Decay in orbit, or DIO, electrons are not the result of muon-to-electron observed conversion, so the tracker must discard them.

Chapter 2

Tracker design

Tracker mechanical design is almost accomplished, even though some aspects and features are still subject of debate among experts and managers. I will speak about the current state of the art.

2.1 Tracker frame

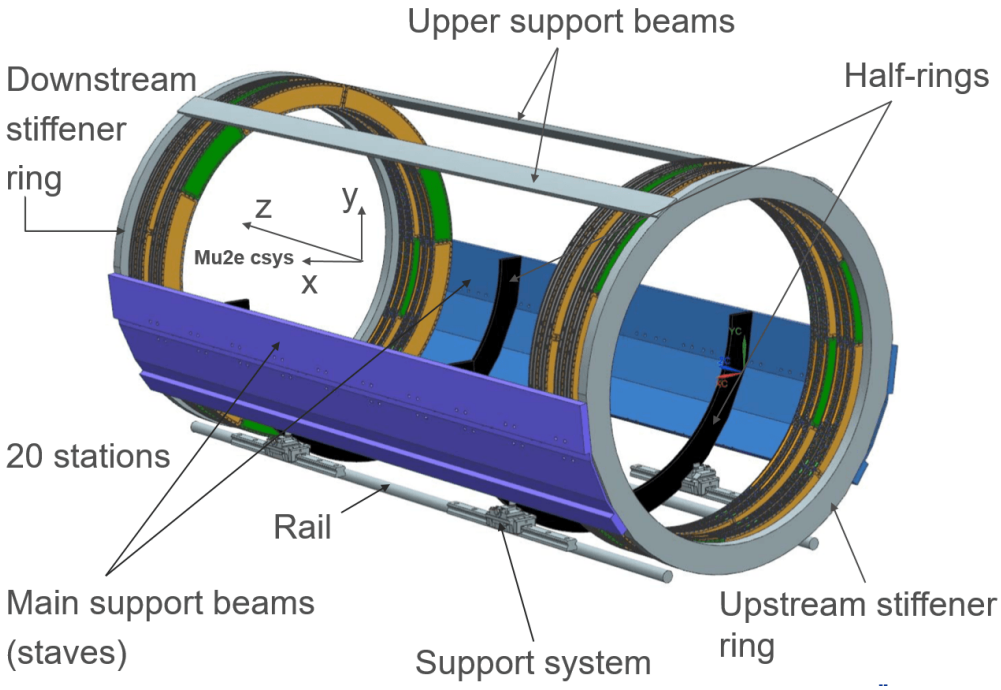

Figure 2.1: Tracker frame components; Mu2e coordinates system is shown.

Twenty stations (in fig. 2.1 only four are present to better show other elements), all equal and coaxial, make up the tracker [2]. The support structure, called *frame*, is

composed of two stiffener rings, upstream and downstream, two lateral main support beams, *staves*, and two upper support beams. Other two half-rings permit to constrain the tracker to rails, so that it can be moved along its axis and it is electrically isolated.

2.2 Panel, plane, station

The key component of a station is the panel, made of aluminum, inside which 96 straws (par. 2.3), disposed on two parallel layers, are contained [3].

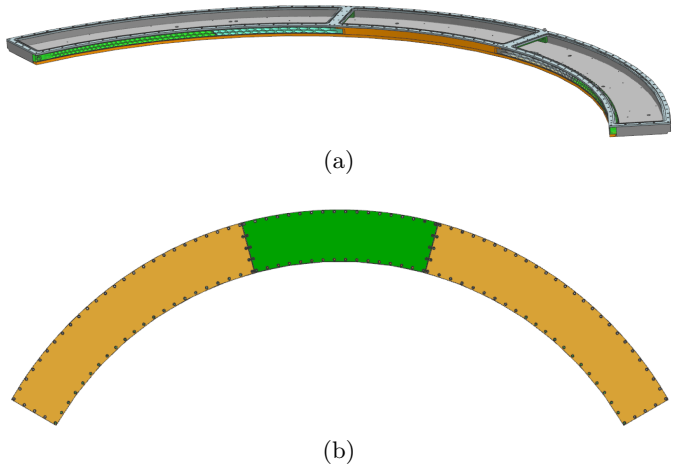

(a)

(b)

Figure 2.2: Views of panel.

As the central angle of each panel is 120°, three concentric panels shape a ring, named *face*; considering two faces whose angular difference, from front to back, is 30° around tracker axis, a plane is obtained (fig. 2.3 (a)). Two planes, where one of them is oriented at 180° around the vertical axis, define a station (fig. 2.3 (b)).

2.3 Straw

The basic detector element of the tracker is the 5 mm diameter straw (in fig. 2.4 the whole assembly is represented) [3]. It is a tube made of 15 µm thick metalized Mylar®: among two layers of 6.25 µm Mylar®, a layer of adhesive is inserted. The inner surface has a 200 Å gold layer over 500 Å aluminum (cathode layer), while the outer has 500 Å aluminum layer, to supply more electrostatic shielding and improve leak rate.

The straw contains a coaxial 25 µm diameter gold plated tungsten sense wire and a blend of Ar:CO_2 (80:20) as drift gas. Straws and sense wires are respectively tensioned to 500 g and 80 g. Fig. 2.5 shows a complete station, with straws.

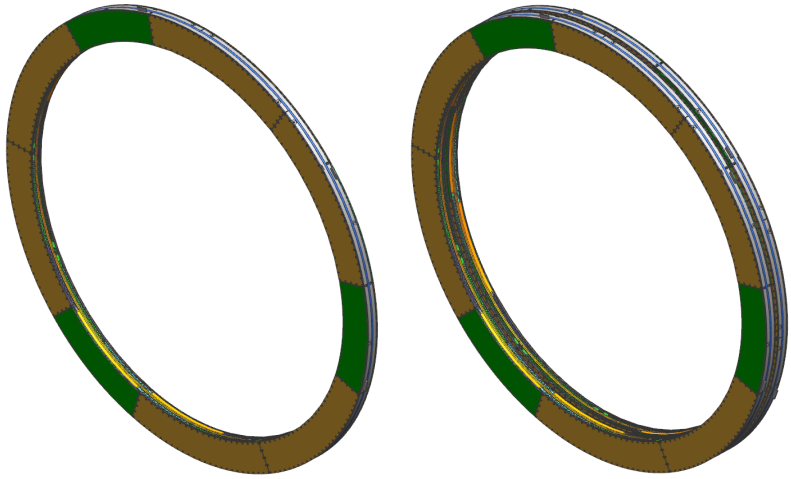

(a) (b)

Figure 2.3: Plane (a) and station (b).

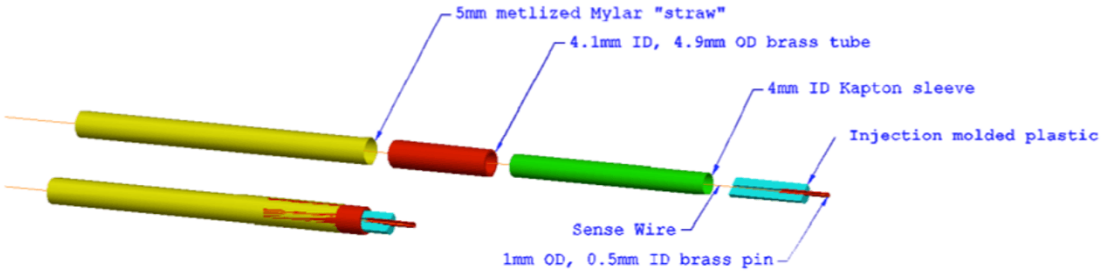

Figure 2.4: Straw and relative equipment, exploded and assembled.

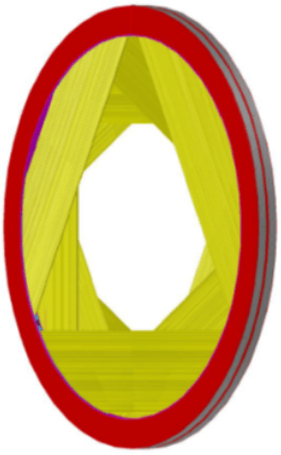

Figure 2.5: Station with straws.

Chapter 3

Conceptual design of electrical and gas system

As described on the previous chapters, the mechanical design was finalized after that stiffness, stress and manufacturing costs had been optimized through a detailed analysis. The main mechanical and structural interfaces had to be examined.

As a consequence, layout and interfaces of electrical and gas lines needed to be designed surrounding the established structural design.

3.1 Electrical system layout

3.1.1 HV and Ear slots

We started listing the main required components for electrical system (fig. 3.1):

- Motherboard, with all electrical circuits;
- Low Voltage (LV) card (*Key*);
- High Voltage (HV) card;
- Ear, a simple printed circuit board to expose the signals inside the panel, to whom the Key is plugged in.

At the very beginning, we created slots on panel lateral surface to make room for HV card and Ear: they needed to communicate with the motherboard inside the panel. The motherboard itself was bonded to the panel baseplate through fasteners[1].

[1]Washers diameter has still to be determined: assuming that motherboard is in contact only with washers, not directly with the baseplate, an analysis of motherboard and baseplate geometrical tolerances is necessary before choosing exact washer dimensions.

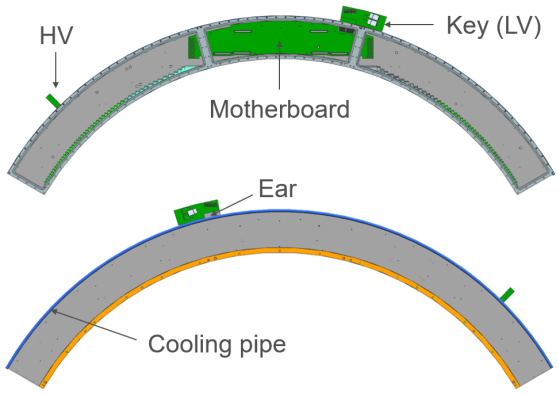

Figure 3.1: Front and back view of a panel, with electrical tools. To be thorough, even cooling pipe is represented: it is a simple representation, because cooling system analysis has still to begin.

3.1.2 Panel cables layout: wires direction

Afterwards, Key and HV cables had to be schematized; the design envisaged that each panel had to be served regardless of others, so that they were at the same time independent and isolated in any case of electrical breakdown.

To work, each Key needed:

- # 32 20 Ga square wires[2];
- # 6 fiber wires, $\phi_j = 2\,\mathrm{mm}^3$.

To reduce their encumbrance, they all followed circumferential direction, keeping in contact with panel lateral surface (fig. 3.2 (a)).

HV card, instead, required one single wire[4] which still moved circumferentially but leant on panel cover, not on its lateral surface: it had also to make for radial and axial direction to reach every panel (fig. 3.2 (b)).

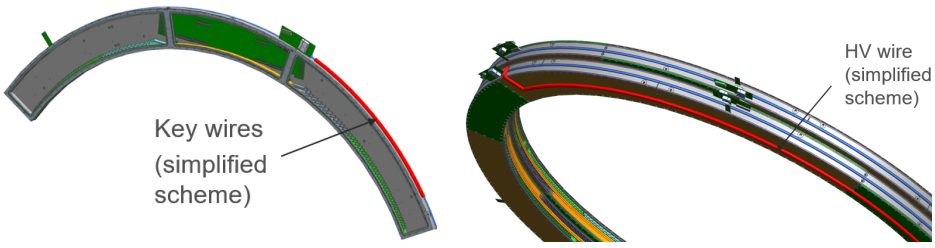

(a) (b)

Figure 3.2: Key (a) and HV (b) wires layout.

[2]Side = 0.812 mm.
[3]Jacket diameter.
[4]Wire diameter hasn't been established yet.

3.1.3 Panel cables layout: constraints

Our aim was to figure out an optimal section for Key wires (given that HV card needed just one cable, its section was given after choosing its diameter), in agreement with space and technological constraints.

Space constraints Since we had to deal with a cylindrical geometry, we considered constraints along axial (z-axis)(fig. 2.1), circumferential and radial direction.

As for z-axis, we had to highlight plane thickness, 47 mm, laser tracking spheres encumbrance[5], 14 mm, and the minimum distance between Keys and HV cards, 17 mm.

While there weren't particular constraints along circumferential direction, the main constraint regarding radial direction was the minimum distance between fiber connector[6] and panel lateral surface, 15 mm.

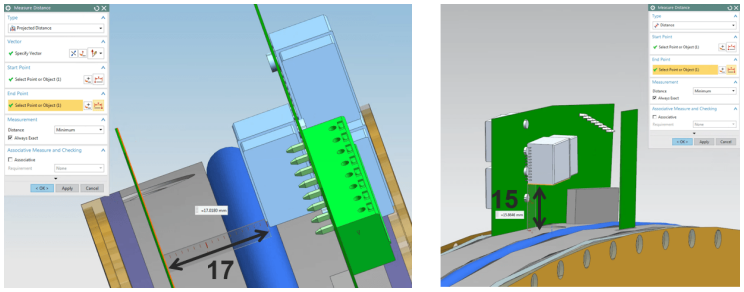

(a) (b)

Figure 3.3: Minimum distance between Keys and HV cards (a) and minimum distance between fiber connector and panel lateral surface (b).

Technological constraints The most significant technological constraint was due to fiber wire: in fact, to work properly, each cable required a minimum bending radius, r_b, about ten times fiber core diameter[7], ϕ_c. As a consequence, being $\phi_c = 750\,\mu m$, we assumed conservatively $r_b = 10\,mm$.

3.1.4 Panel cables layout: section

According to tracker geometry, there were six Key-HV card groups[8] for each panel; every group needed to be served by relative electrical wires, whose position, along circumferential direction, is reported in fig. 3.4.

[5] To assure planes mutual alignment while inserted into the frame, laser tracking technology is employed. Holes are created on panel lateral surface to host spheres.

[6] Fiber wires are connected to Key through fiber connectors: each hosts two fiber wires, so there are three connectors on each Key.

[7] As suggested by electrical devices experts.

[8] Key and HV card align along tracker axis.

In the bottom circle, two bundles, belonging to different groups, overlap, so that the worst condition, namely the condition of maximum encumbrance (shown in fig. 3.4 through letter D), is obtained.

The optimal cables section is reported in fig. 3.5.

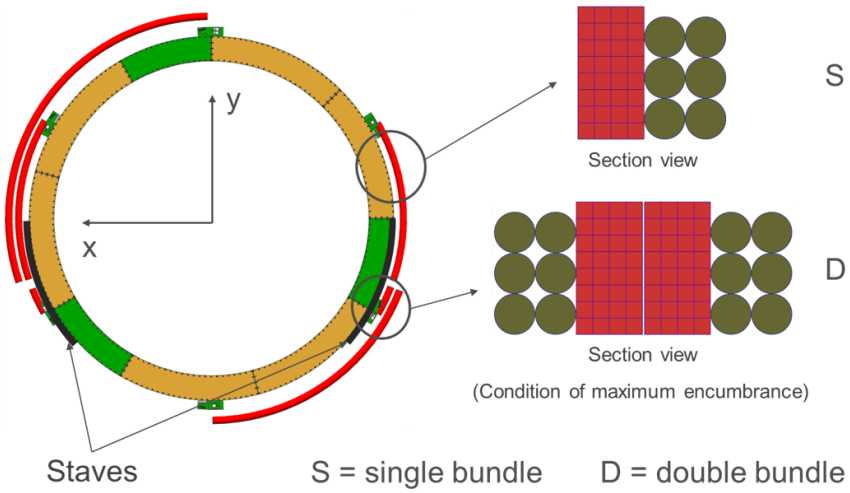

Figure 3.4: Circumferential disposition of Key wires, highlighted in red. The radial position is not the correct one, as they are actually in contact with panel lateral surface; they are represented in this way to better display their angular position.

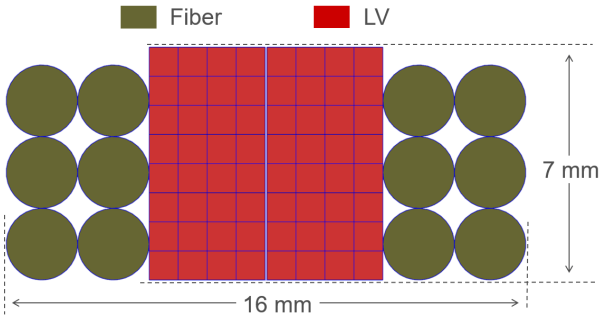

Figure 3.5: Fiber and LV cables section view.

From fig. 3.6 it is possible to observe that space and technological constraints were respected. We used 16×8 mm^2 as cables section dimensions (and not 16×7 mm^2 as pointed out in fig. 3.5) because of the presence of cooling line (fig. 3.1), which was in contact with Key wires and might increase the final encumbrance. The addition of 1 mm was conservative.

According to the model above, the overall radial encumbrance was 868 mm (fig. 3.7), which exceeded the maximum design value of 850 mm [2]. Due to this, it has still to be understood whether the proposed layout could be employed or not.

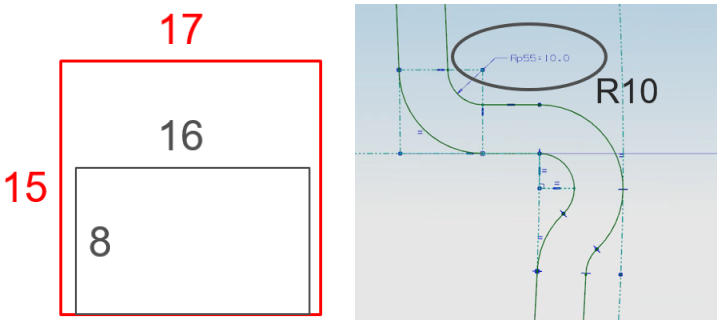

(a) (b)

Figure 3.6: Respect of space (a) and technological constraints (b).

3.1.5 Stave axial groove slots

Fig. 2.1 shows left and right staves intact, although slots on their axial groove had to be conceived in order to make room for Keys and HV cards: they wouldn't have had space to be installed on each panel (fig. 3.8). We have to specify that slots shape was rough and temporary: it was useful to underline the matter, but its dimensions were not the result of particular calculations[9].

3.1.6 Axial groove cables layout

Once cables are connected to each Keys and HV cards, they circle the panel and reach staves (fig. 3.4); then they 90° bend and enter axial groove, following z-axis direction (we assumed that cables laying sequence was from upstream to downstream side).

Cables from two stations Analyzing only cables belonging to two stations (fig. 3.9), our layout considered space and technological constraints; slots dimensions were tentative, so this mock-up was a starting attempt.

Cables from twenty stations While cables of consecutive stations are placed along axial groove, from upstream to downstream, they necessarily overlap, given that the maximum width of allowable region is 130 mm (fig. 3.9 (a)). Our target was to minimize the radial encumbrance due to wires overlapping, which occurred at downstream side, where cables of all twenty stations were gathered. Cables section view at downstream side (app. A) is shown in fig. 3.10.

The maximum radial encumbrance, in agreement with this model, was 888 mm, even bigger than 868 mm: as already written (par. 3.1.4) further evaluations have to be done. For example, the possibility of employing more space (fig. 3.11), modifying electrical devices shape, could be taken into consideration.

[9]Before completing design of slots shape, Finite Elements Analysis (F.E.A.) has to be run to evaluate the impact on staves stiffness.

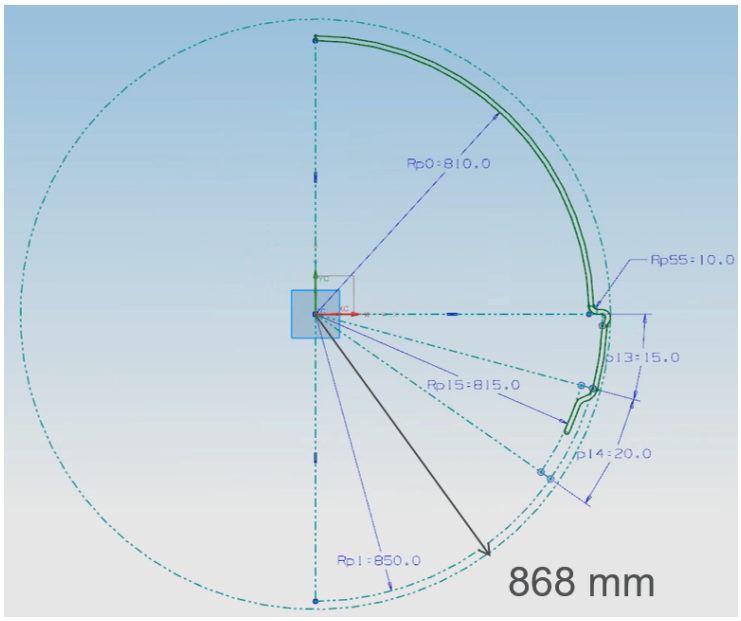

Figure 3.7: Key wires overall radial encumbrance.

3.2 Gas system layout

To supply gas (par. 2.3) to straws, a pipeline had to be figured out. The main requirement to satisfy was that each panel should have been isolated, so that, in any case of leakage, other panels would have been able to keep on working.

To start with, these elements were necessary (fig. 3.12): # 1 main inlet axial pipe, # 1 main outlet axial pipe and an optimizable[10] number of circumferential and radial pipes to reach every panel.

A tentative layout, shown in fig. 3.13, was developed; employed diameters were approximate, they will be probably decided when:

- HV wire diameter (fig. 3.2 (b)) is fixed, to respect the principal space constraint, namely the gap between each station[11];
- Gas pressure for each pipe is determined.

3.3 Cables fixing

What discussed until now would be correct as long as we managed to fix cables and pipes position. To achieve this result, we could choose from two generally adopted solutions:

[10] Gas system design needs still lots of development.

[11] As HV wire and circumferential pipe stay in contact with panel covers, they will be positioned between stations.

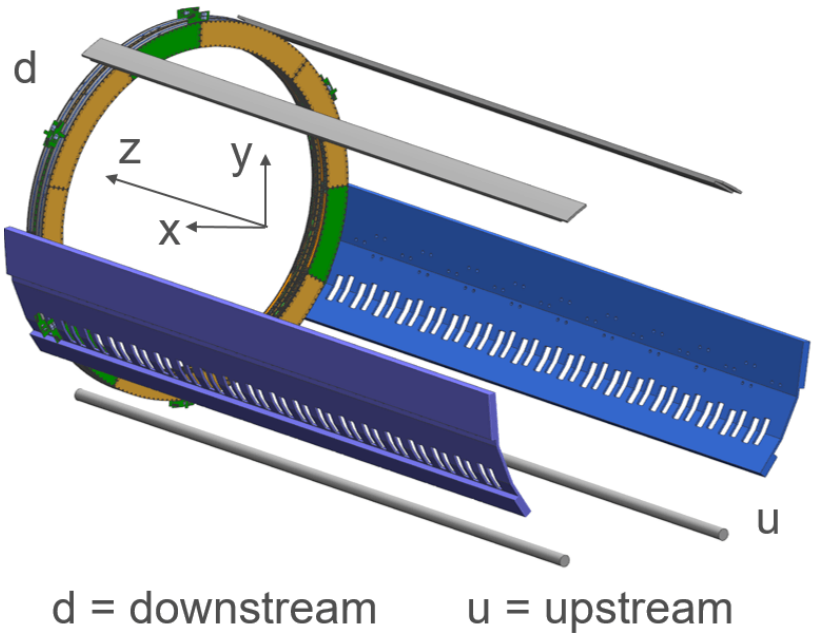

(a)

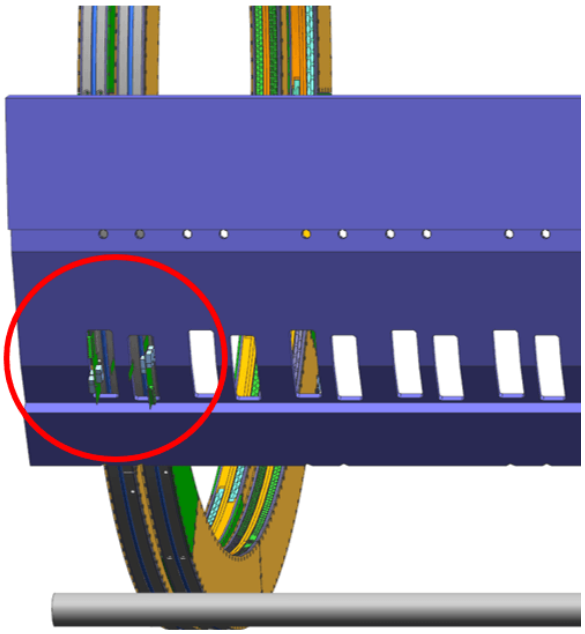

(b)

Figure 3.8: Slots on stave axial groove (a) and relative enlargement (b).

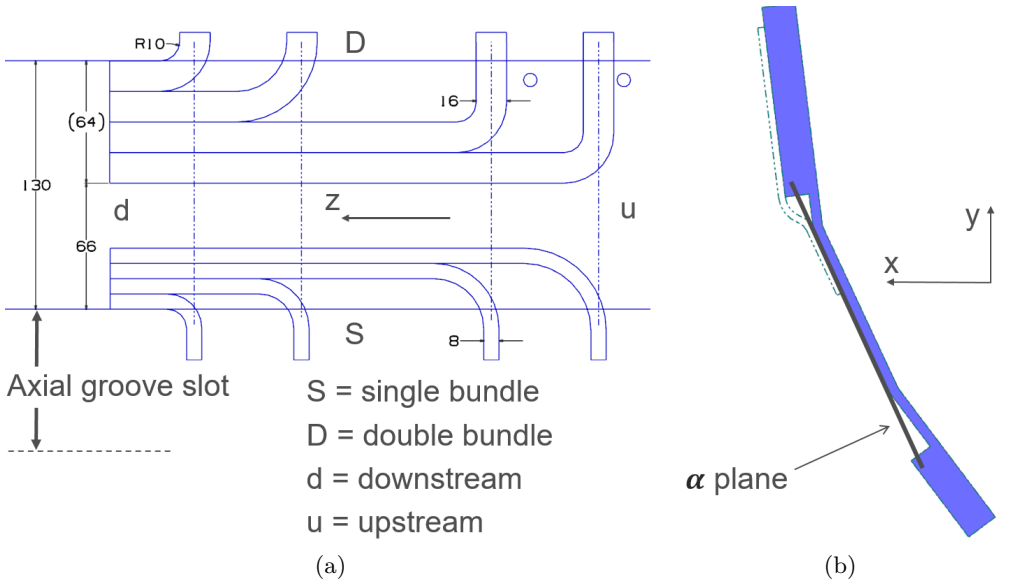

Figure 3.9: Cables layout for two stations (α plane view) (a) and position of α plane (b).

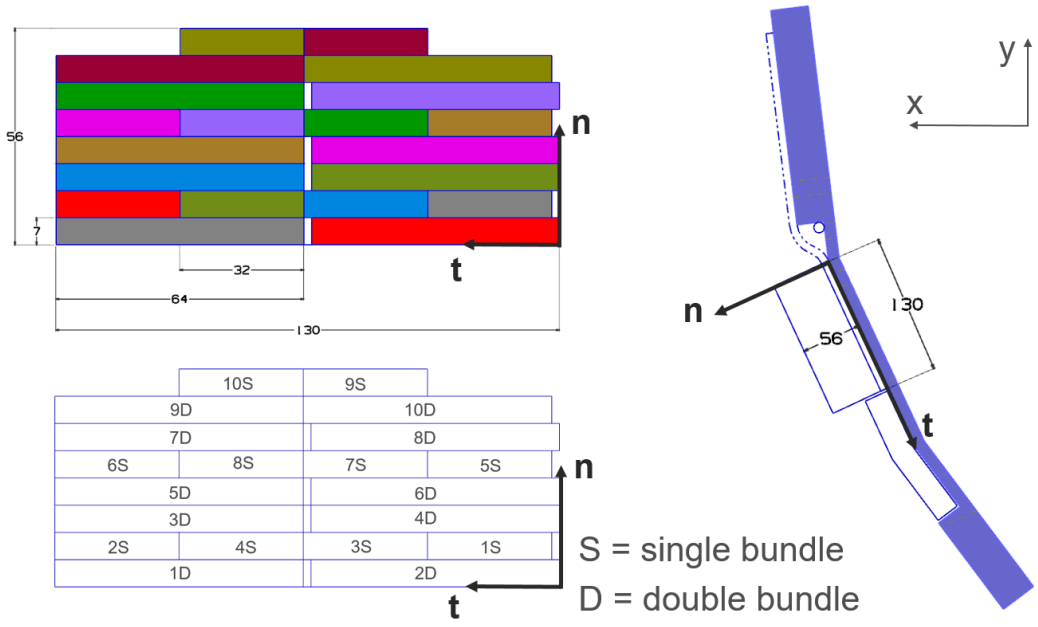

Figure 3.10: Key and HV wires section view at downstream side. Cables are divided into ten groups: each group represents two consecutive stations. On the top left picture, each color stands for one group; on the bottom left picture, the same scheme is displayed, but a label made of a number and a letter is used: the number symbolizes the group, the letter the type of bundle, single or double.

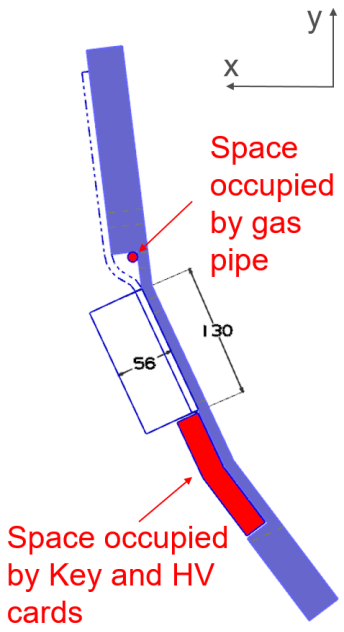

Figure 3.11: We imagined to employ only a 130 mm width, discarding spaces respectively occupied by gas pipe and Keys/HV cards.

vacuum compatible cable ties or vacuum glue. They were both usable and valid, however vacuum compatible cable ties were preferable because of their capability of being more easily removed than vacuum glue. Actually, this may often occur, e.g. to remove or reinsert a plane for maintenance, to replace defective cables, or similar operations.

Among vacuum compatible cable ties, we could select from zip (fig. 3.14 (a)) or mountable cable ties (fig. 3.14 (b)): the former envisaged no further mechanical processes (requested by the latter to create screw holes on panel surface), but we even preferred mountable ties, which assured contact between wires (or pipes) and panel surface.

As for employable materials, we haven't chosen yet between:

- *PEEK* (Polyether ether ketone), able to work up to 10^{-10} Torr;
- Stainless steel, up to 10^{-11} Torr.

The cost was similar and they both succeeded in withstanding DS pressure, which is 10^{-4} Torr (par. 1.2).

To place each mounting cable tie, a vented screw was necessary to work in a medium-vacuum environment (fig. 3.15).

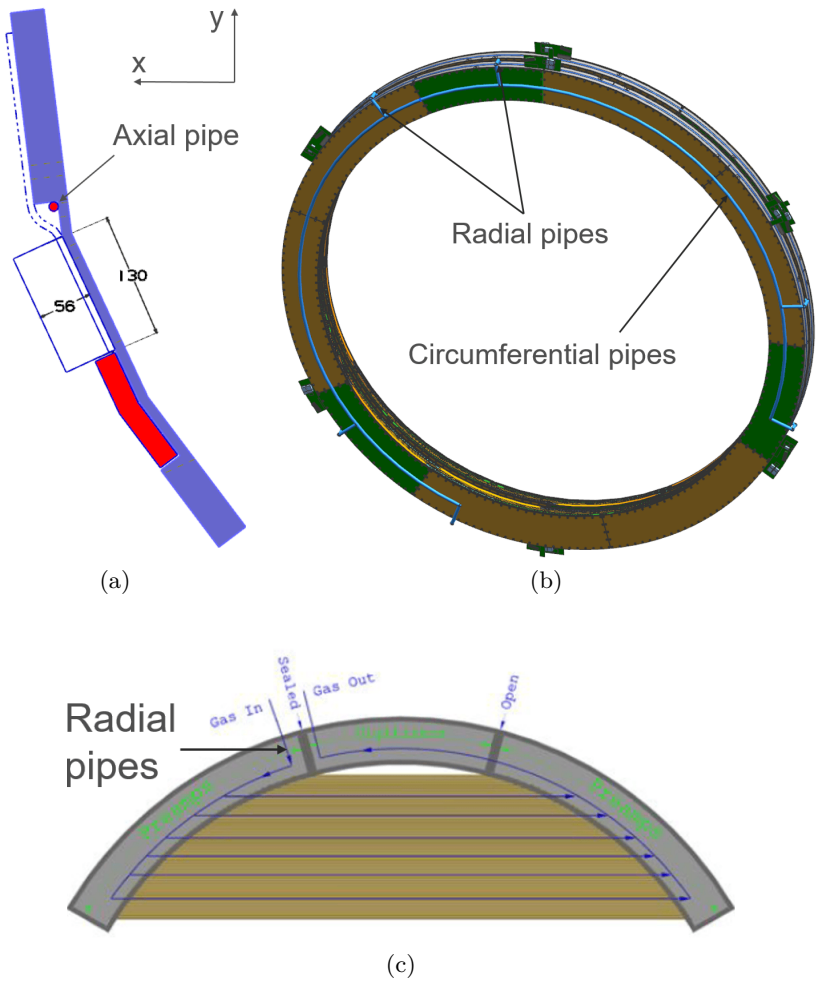

Figure 3.12: Axial (a), circumferential (b) and radial pipes, to install inside the panel manifold (c).

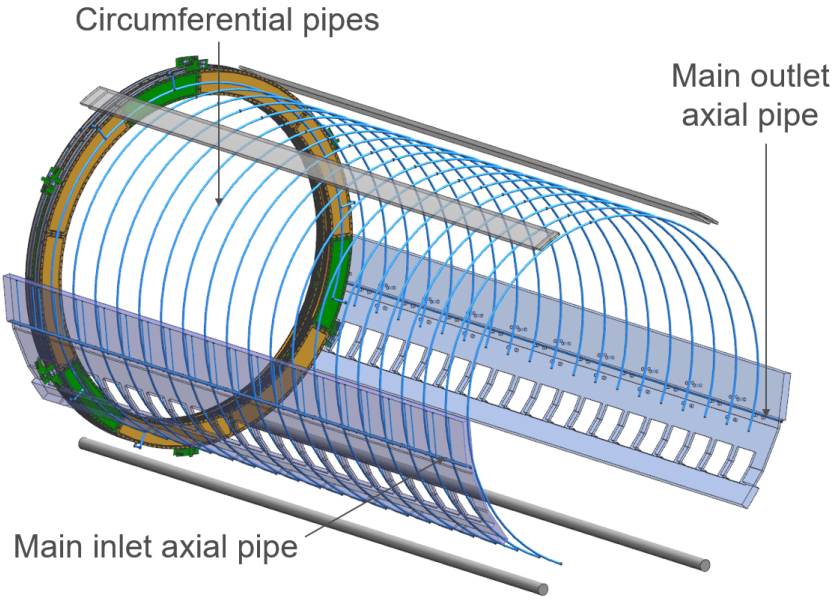

Figure 3.13: Gas system pipeline layout.

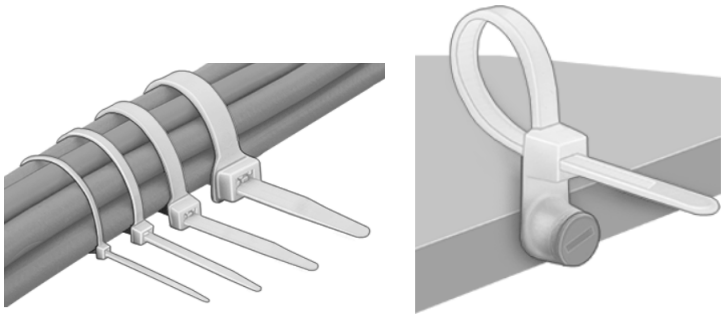

(a) (b)

Figure 3.14: Zip (a) and mountable cable ties (b).

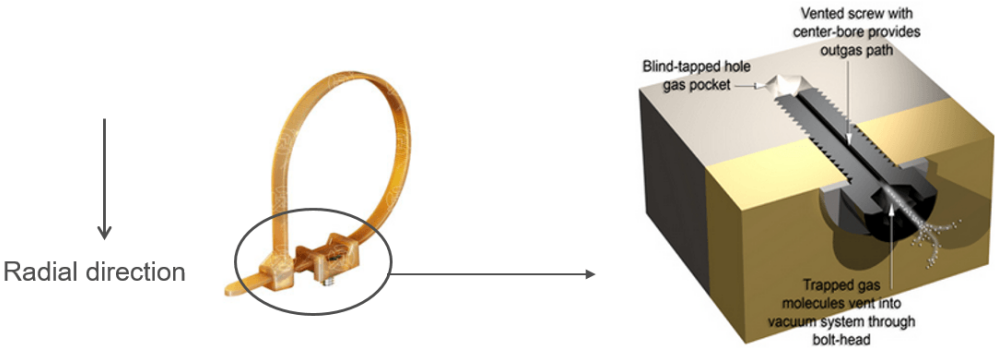

Figure 3.15: Mounting cable tie (a) and relative vented screw (b).

Chapter 4

Analytical evaluation of mounting planes uncertainty

Every plane of the tracker had to be constrained to the tracker frame; ANL[1] proposed a solution, known as *kinematic mount*: through three points of contact, whose angular position is respectively $\beta = 0$, π and $3\pi/2$ (fig. 4.1 (a)), the plane has its six degrees of freedom (DOF) removed[2]. In our case, three spheres are soldered to the plane, while three grooves are obtained on the inner surface of the frame and on a bottom rack (fig. 4.1 (b)).

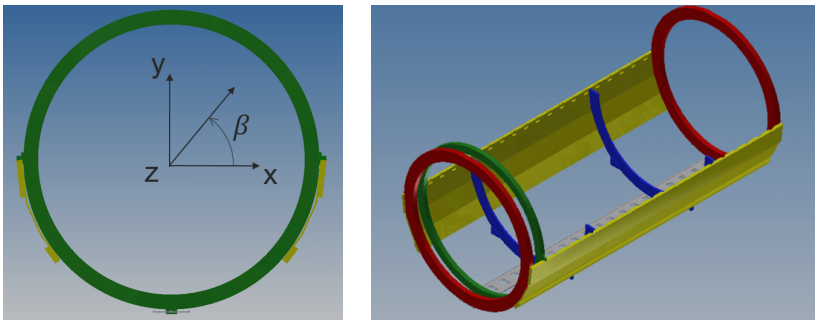

(a) (b)

Figure 4.1: Spheres position (a) and simplified scheme of the tracker frame (b).

The idea of kinematic mount offers two important advantages:

1. The constrain is isostatic, so there is no stress due to heat or assembly errors;
2. It is possible to remove and reinsert planes to the same position with high accuracy (repeatability of 100 µm, see app. B).

[1] Argonne National Laboratory, USA.

[2] The two grooves at 0° and 180° remove motion along z-axis and y-axis and rotation around z-axis; the bottom groove eliminates the three left DOF.

4.1 Misalignment between spheres and grooves

When planes are inserted for the first time in the frame, or when maintenance is necessary (planes removed and reinserted), spheres position and grooves direction has to match, to assure mutual alignment. Unfortunately, both are affected by errors, so that there is misalignment. To simplify our analysis, we assumed that only grooves direction was affected by errors, while spheres position was still the same.

Our aim was to find the geometrical configuration, namely the angular position of each point of contact, which minimized the misalignment between spheres and grooves.

4.2 Analytical evaluation of misalignment

At first, assuming $i = 1, 2, 3$, we wrote the initial geometry for spheres (eq. 4.1) and grooves (eq. 4.2), as shown in fig. 4.2:

$$(x_i, y_i) = R_i(\cos\theta_i, \sin\theta_i) \tag{4.1}$$

$$x_i = (\cot\alpha_i)y_i \tag{4.2}$$

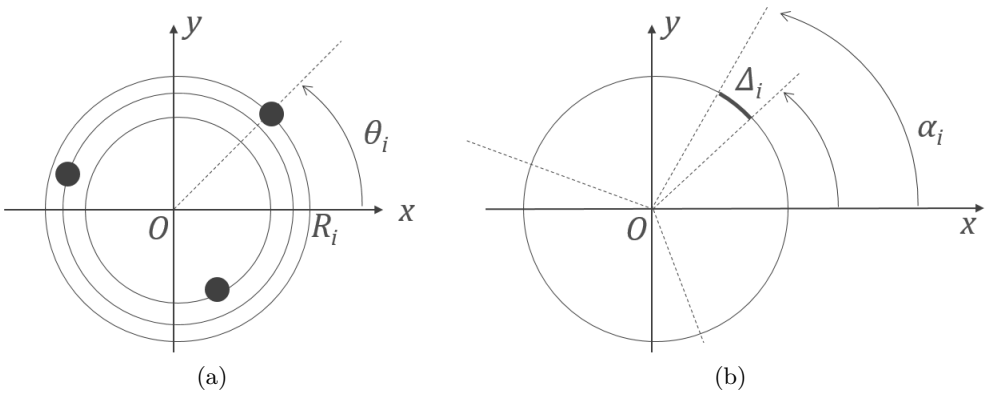

Figure 4.2: Spheres positions (a) and grooves directions, affected by errors (b).

We translated and rotated spheres coordinate system, in order to align them to the respective grooves direction [4]

$$\begin{pmatrix} \bar{x_i} \\ \bar{y_i} \end{pmatrix} = \begin{pmatrix} \cos\theta & -\sin\theta \\ \sin\theta & \cos\theta \end{pmatrix} \begin{pmatrix} x_i + x_0 \\ y_i + y_0 \end{pmatrix} \approx \begin{pmatrix} 1 & -\theta \\ \theta & 1 \end{pmatrix} \begin{pmatrix} x_i + x_0 \\ y_i + y_0 \end{pmatrix} \approx \begin{pmatrix} x_i + x_0 \\ y_i + y_0 \end{pmatrix} \tag{4.3}$$

The approximation above is acceptable because $x_0, y_0, \theta R \leq 0.1\,\text{mm}$.

According to alignment condition, we could state that:

$$\bar{x_i} = (\cot \alpha_i)\bar{y_1} \tag{4.4}$$

$$\alpha_i = \theta_i + \frac{\Delta_i}{R_i} \tag{4.5}$$

Substituting eq. 4.3 in eq. 4.4, we obtained:

$$-x_0 + (\cot \alpha_i)y_0 + \theta[(\cot \alpha_i)x_i + y_i] = x_i - (\cot \alpha_i)y_i \tag{4.6}$$

Besides:

$$\cot \alpha_i = \cot(\theta_i + \frac{\Delta_i}{R_i}) \approx \cot \theta_i - \frac{\Delta_i}{R_i \sin^2 \theta_i} \tag{4.7}$$

where we expanded in series ($\Delta_i/R_i \ll 1$) and held only first order terms.
Because of eq. 4.7, from eq. 4.6 we shifted to eq. 4.8:

$$-x_0 + (\cot \theta_i)y_0 + \frac{\theta R_i}{\sin \theta_i} = \frac{\Delta_i}{\sin \theta_i} \tag{4.8}$$

We could also add that: $R_i = R + \Delta R_i$, with $\Delta R_i \leq 1\,\text{mm}$; so we had that: $\theta R_i \approx \theta R$ because $\theta \Delta R_i$ is a second order term.
We eventually got to the final equation:

$$-x_0 \sin \theta_i + y_0 \cos \theta_i + \theta R = \Delta_i \tag{4.9}$$

whose respective matrix format is:

$$\begin{pmatrix} -\sin\theta_1 & \cos\theta_1 & 1 \\ -\sin\theta_2 & \cos\theta_2 & 1 \\ -\sin\theta_3 & \cos\theta_3 & 1 \end{pmatrix} \begin{pmatrix} x_0 \\ y_0 \\ \theta R \end{pmatrix} = \begin{pmatrix} \Delta_1 \\ \Delta_2 \\ \Delta_3 \end{pmatrix} \tag{4.10}$$

4.3 Reduction of number of independent variables

We had three variables $(\theta_1, \theta_2, \theta_3)$ to come up with. In order to obtain only one independent variable, some assumptions can be listed, looking at fig. 4.3:

- To gain stability, it was necessary to have one sphere on the negative side of y-axis and two on the positive side;
- A symmetrical configuration was preferable, so that, if spheres 1 and 2 were identical, centroid would be theoretically located on y-axis.

As a result, we had that:

$$\theta_2 = \pi - \theta_1$$

$$\theta_3 = \frac{3}{2}\pi$$

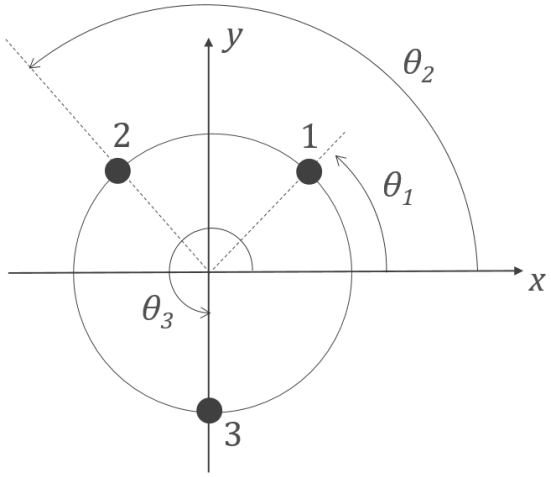

Figure 4.3: Representation of $\theta_1, \theta_2, \theta_3$ according to assumptions above.

with a constraint about θ_1:

$$0 \leq \theta_1 < \frac{\pi}{2}^3 \tag{4.11}$$

Eq. 4.10 turned into eq. 4.12:

$$\begin{pmatrix} -\sin\theta_1 & \cos\theta_1 & 1 \\ -\sin\theta_1 & -\cos\theta_1 & 1 \\ 1 & 0 & 1 \end{pmatrix} \begin{pmatrix} x_0 \\ y_0 \\ \theta R \end{pmatrix} = \begin{pmatrix} \Delta_1 \\ \Delta_2 \\ \Delta_3 \end{pmatrix} \tag{4.12}$$

4.4 Variation region of x_0 and y_0

Let's briefly focus on Δ_i, the i-arc length which constitutes the error on i-groove direction. It was possible to state that:

$$-\frac{\Delta}{2} \leq \Delta_i \leq \frac{\Delta}{2} \tag{4.13}$$

where $\Delta = 10\,\mu\text{m}$ (app. B).

In agreement with eq. 4.13, from eq. 4.12 we got a linear system made up of three inequalities:

$$\begin{cases} -\Delta \leq (-\sin\theta_1 - 1)x_0 + \cos\theta_1 y_0 \leq \Delta & (4.14) \\ -\Delta \leq (-\sin\theta_1 - 1)x_0 - \cos\theta_1 y_0 \leq \Delta & (4.15) \\ -\Delta \leq 2\cos\theta_1 y_0 \leq \Delta & (4.16) \end{cases}$$

Considering a $x_0 - y_0$ plane, the linear system can be represented by an area, as displayed in fig. 4.4, that is the allowable variation region for x_0 and y_0, parameters of the translation above (eq. 4.3).

[3] $\pi/2$ can't be accepted because it would mean that spheres 1 and 2 overlap.

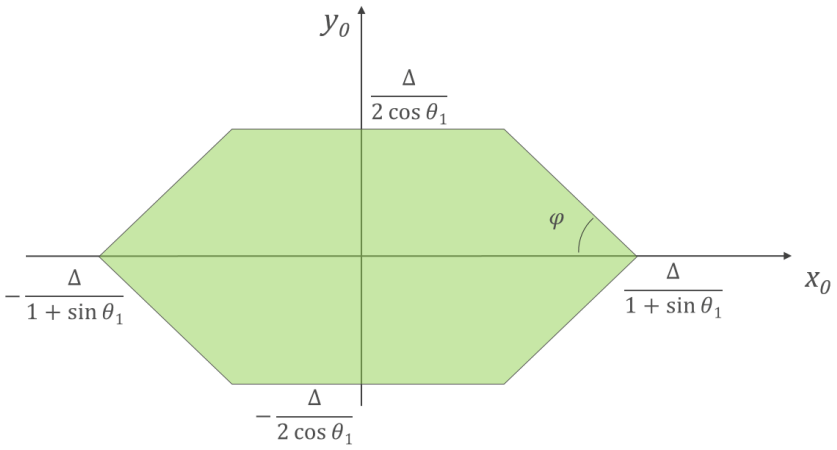

Figure 4.4: Variation region of x_0 and y_0. It is helpful to add that: $\tan\varphi = \frac{1+\sin\theta_1}{\cos\theta_1}$.

4.5 Misalignment minimization

The wider the variation region is, the higher misalignment we get, so we would have managed to minimize it if the area of the variation region had been minimum. Given that this area is function of only one variable, θ_1, it was sufficient to evaluate its expression and look for the value of θ_1 for which it was minimum.

If $A(\theta_1)$ is the area of the variation region, we have:

$$A(\theta_1) = \frac{3}{2}\frac{\Delta^2}{(1+\sin\theta_1)\cos\theta_1} \tag{4.17}$$

It's not difficult to prove that $A(\theta_1)$ is minimum when $\theta_1 = \pi/6$ (respecting eq. 4.11).

4.6 Comparison between ideal and Argonne's configuration

From this moment on, *ideal* configuration has to be meant as the configuration according to which:

$$\begin{pmatrix}\theta_1\\ \theta_2\\ \theta_3\end{pmatrix} = \begin{pmatrix}\pi/6\\ 5\pi/6\\ 3\pi/2\end{pmatrix} \tag{4.18}$$

while Argonne's configuration is, as already mentioned:

$$\begin{pmatrix}\theta_1\\ \theta_2\\ \theta_3\end{pmatrix} = \begin{pmatrix}0\\ \pi\\ 3\pi/2\end{pmatrix} \tag{4.19}$$

Fig. 4.5 shows that ideal configuration region is less than Argonne's region. In particular, while along y_0-axis the displacement is a bit wider, along x_0-axis Argonne's expected displacement is 50% higher than ideal.

This aspect should have convinced us to adopt the ideal configuration; nevertheless, Argonne's proposal could be accepted and realized[4]. But why adopting a configuration that produces a larger misalignment? The answer might be summarized as follows:

- From a technical point of view, it isn't even possible to insert planes inside the tracker frame, if grooves are placed at $\pi/3$ and $5\pi/6$; it would be much easier to install all planes (on another structure?) and than assemble the frame around;
- Still assuming to succeed into mounting planes on the frame, staves stiffness would be probably lowered[5].

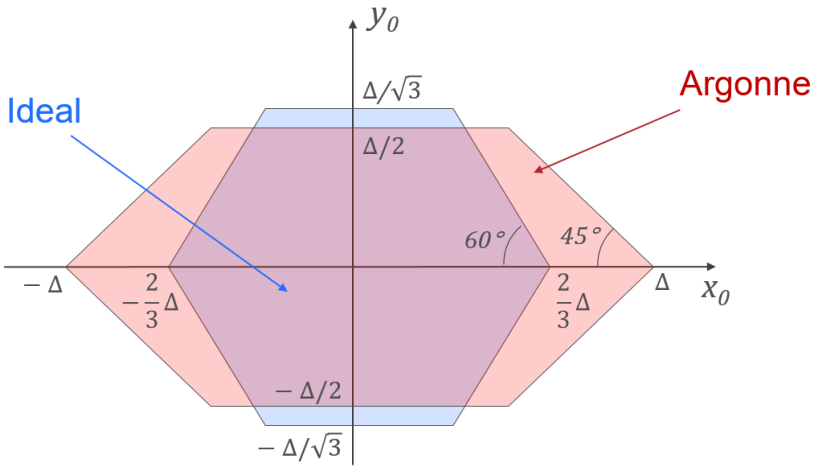

Figure 4.5: Comparison between ideal and Argonne's configurations.

[4]Further analysis has to be carried out.
[5]More studies are necessary to confidently state this sentence.

Chapter 5

Planes contact pressure analysis

After kinematic mount concept, Argonne suggested to consider cylindrical grooves; therefore, for each plane support point we had a sphere-cylindrical groove contact.

5.1 Use of HertzWin®software

To obtain a simple estimation[1] of contact pressure, Argonne employed HertzWin®software[2] (in fig. 5.1 its main screen is inserted).

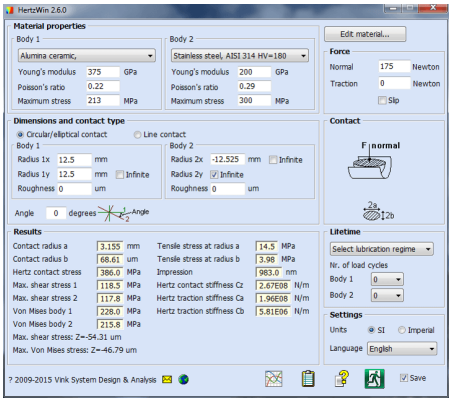

Figure 5.1: Main screen of HertzWin®software.

Before taking into account any calculations, we tested the software: starting with the same geometrical input data, we compared its results with those obtainable through the application of Hertz's formulas, e.g. contact between two spheres and two cylinders. Output data matched almost perfectly (differences of $3 \div 5\%$, maybe also due to the fact that the values to insert in analytical formulas were not precise but already approximated).

[1] It is understood that final design will have to agree to F.E.A. results.
[2] Software developed by Vink System Design and Analysis.

5.2 Argonne's attempts

Argonne proposed at first [5]:

- $R_s = 9.525\,\text{mm}$, structural stainless steel ($\sigma_y = 290\,\text{MPa}$)[3];
- $R_{cg} = 9.600\,\text{mm}$, same material as sphere.

where R_s and R_{cg} respectively stand for sphere and cylindrical groove radius.

Yet, Von Mises's stress, evaluated through the software, produced a corresponding safety factor (SF) of 1.01, which didn't seem to be acceptable[4].

As a second try, they changed materials maintaining the same geometry:

- $R_s = 9.525\,\text{mm}$, silicon-nitride ceramic ($\sigma_y = 1000\,\text{MPa}$);
- $R_{cg} = 9.600\,\text{mm}$, structural stainless steel, coated with WC[5] ($\sigma_y = 3000\,\text{MPa}$).

According to the new configuration, Von Mises's critical point, placed on sphere surface, is 344 MPa, whose SF = 2.91, is widely acceptable.

5.3 Our attempt

So huge a SF actually envisaged an *overquality* problem: too material was employed, whereas less resources were still satisfying, from a safety point of view. As a result, we run a sensitivity analysis to understand which might have been the minimum geometric dimensions able to guarantee, at the same time, an acceptable SF.

After various attempts, the software pointed out that, with $R_s = 4.850\,\text{mm}$ and $R_{cg} = 4.900\,\text{mm}$, using same materials as above, a SF = 1.68 could be obtained. Given that such SF is acceptable, this configuration may be confirmed and adopted.

Fig. 5.2 shows, for each pattern, the evolution of Tresca's and Von Mises's equivalent stresses, functions of depth (measured from contact surface). The order of magnitude of the depth in correspondence of which maximum stress is reached is $10 \div 100\mu\text{m}$.

Therefore, next steps may require a choice of different materials for each sphere (as already happens for cylindrical groove): a high-resistance coating to sustain surface contact, and a more ductile material when stress level is lower.

[3] Compressive yield strength.

[4] While SF has to be, for most applications, at least $1.2 \div 1.3$, in this particular case also SF ≈ 1 may be tolerate. In fact, even though plasticity appears, this phenomenon is local and doesn't affect the whole body. Nevertheless, to be conservative, SF ≈ 1 won't be accepted.

[5] Tungsten carbide.

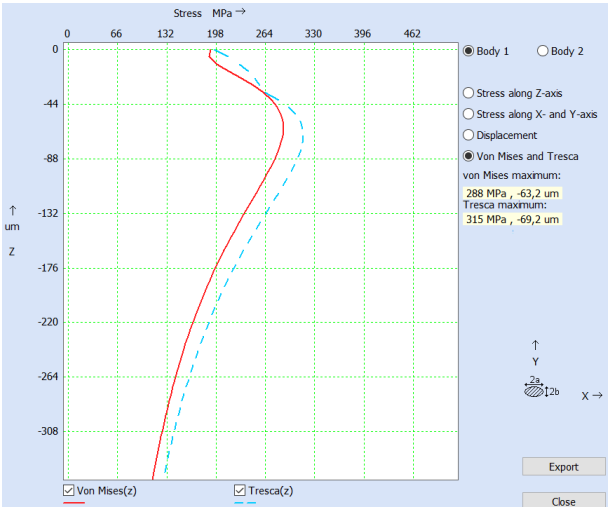

(a)

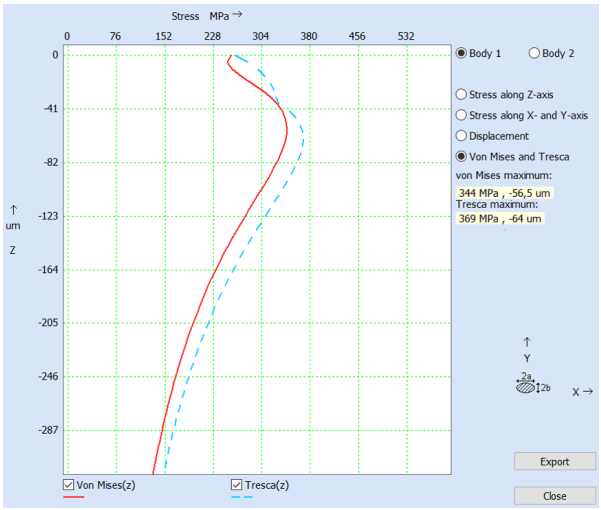

(b)

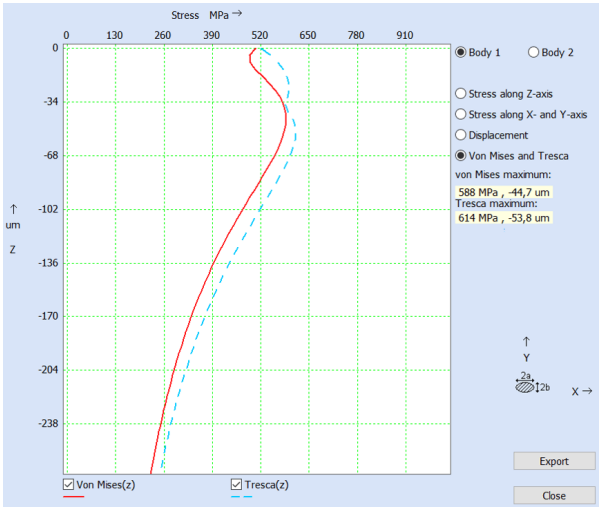

(c)

Figure 5.2: Evolution of Tresca's and Von Mises's stresses, functions of depth, according to Argonne's first proposal (a), second (b) and our attempt (c).

Chapter 6

Conclusions

In conclusion, the conceptual design of electrical system is obtained, whereas some details need to be evaluated before turning into the proposal design. Gas system layout is at early stage, because some requirements and specifications have still to be considered prior to proceeding on detailed design level.

Argonne's plane support concept was studied in all its principal aspects and it is ready to be developed into proposal design, providing detailed CAD models and official production drawings.

Appendix A

Downstream wires section

To complete cables section analysis at downstream side (par. 3.1.6), we insert fig. A.1, which represents wires laying sequence, from upstream to downstream.

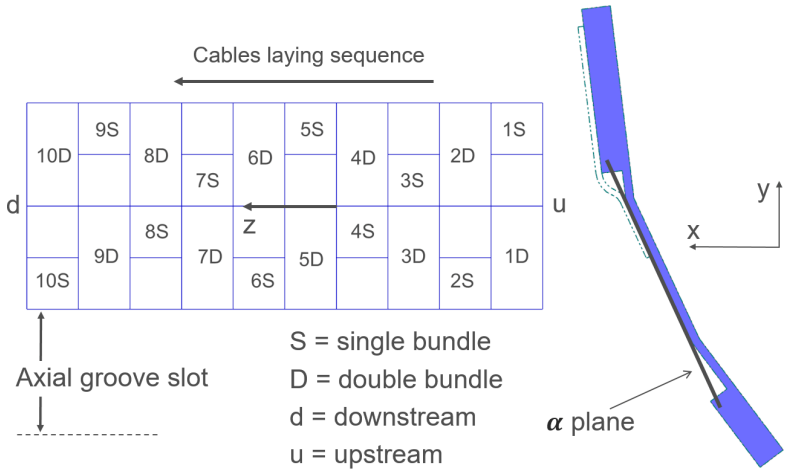

Figure A.1: Cables laying sequence, from upstream to downstream. To refer to each wire, the same label shown in fig. 3.10 is employed.

On left picture, we see that, moving along z-axis, the position of single and double bundles always switches from top to bottom side: e.g. 1S is located on y-axis positive side, while 2S on negative side.

According to this layout, wires disposition has to be mirrored every group, as displayed in fig. A.2.

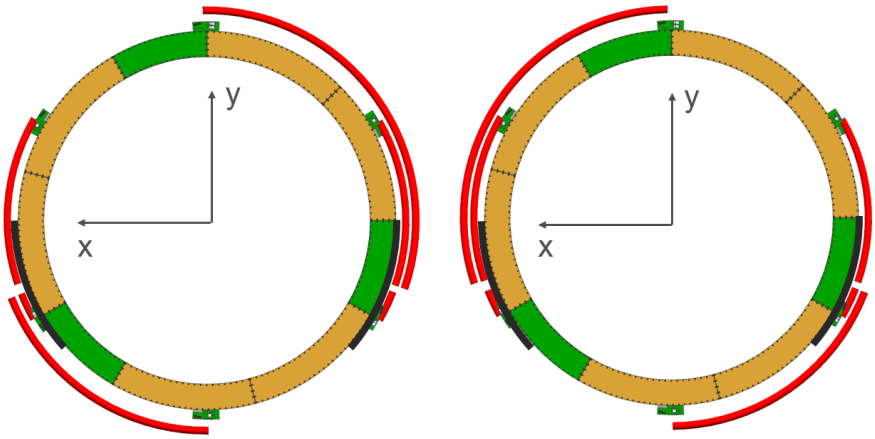

Figure A.2: Every group (two stations) cables disposition has to be mirrored.

Appendix B

Planes reinsertion repeatability

When a plane is removed and reinserted, it is necessary that it occupies about the same position it had before its removal, otherwise the tracker won't work properly. The established constraint is a repeatability, r, of 100 µm: the new position of each plane center must be included in a 100 µm radius circle, whose center corresponds to the old position of plane center (fig. B.1).

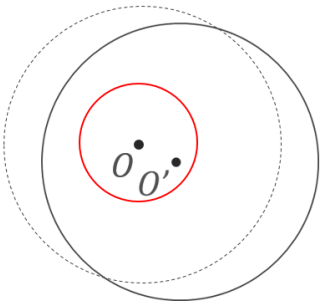

Figure B.1: Representation of repeatability: old plane center (O), new plane center (O') and 100 µm radius circle, centered in O.

Two are generally the elements which produce change of position from O to O':

1. Intrinsic errors, δ, of laser tracking system, through which planes alignment is obtained;
2. Errors, Δ, which affect spheres position and grooves direction.

If we assume $\Delta = 10$ µm (par. 4.4), it is possible to determine the value of δ, remembering that both errors have to be summed up in quadrature:

$$r = \sqrt{\delta^2 + \Delta^2}$$

from which we get:

$$\delta = \sqrt{r^2 - \Delta^2} \tag{B.1}$$

According to eq. B.1, $\delta = 99.5\,\mu m$; it means that errors due to laser tracking system represent the most significant contribution to repeatibility, while errors of spheres and grooves is almost negligible. The chosen value of Δ is therefore valid.

Bibliography

[1] George Ginther, *Mu2e and Muon Beamline Overview*, Doc. DB 6921-v2, March 2016.

[2] Giuseppe Gallo, *Tracker layout*, Doc. DB 4991-v4, April 2016.

[3] Ron E. Ray, *Mu2e Technical Design Report*, Doc. DB 4299-v15, March 2015.

[4] *Error on the V-groove - Analytical approach*, September 2015.

[5] Giuseppe Gallo, Aseet Mukherjee, José Repond, Allen Zhao, *Mu2e Tracker Frame Design*, 2016.